RSC Advances

PAPER

Synthesis of a core/satellite-like multifunctional nanocarrier for pH- and NIR-triggered intracellular chemothermal therapy and tumor imaging†

Xue Yang,‡ Jun Xiong,‡ Pengchao Qiu, Mian Chen, Dinggeng He, Xiaoxiao He,* Kemin Wang* and Jinlu Tang

Here, we have reported a core/satellite-like multifunctional nanocarrier for pH- and NIR-triggered synergistic chemothermal therapy and tumor imaging. In this system, upconversion nanoparticles (UCNPs), which have an average diameter of 23 nm, were first synthesized by a classic high-temperature solvent method and subsequently used as the imaging cores to direct the coating of mesoporous silica shells. The obtained mesoporous silica coated core–shell nanoparticles (UCNP@mSiO$_2$) have a uniform pore size (4.2 nm) and excellent DOX loading ability (85.3 μmol g^{-1} SiO$_2$), which makes UCNP@mSiO$_2$ a good carrier. In order to finally obtain this core/satellite-like system (DOX@UCNP@mSiO$_2$–AuNRs), gold nanorods (AuNRs) with a positive charge of 15 mV were subsequently capped on the negatively charged DOX loaded UCNP@mSiO$_2$ (−30 mV) *via* electrostatic interactions. Under low-pH conditions (*e.g.* pH 4.9), the charge of mesoporous silica changed to −10.8 mV, leading to the separation of AuNRs and the release of entrapped DOX. Moreover, the present AuNRs can effectively convert NIR light (780 nm) into heat, and the increased temperature is as high as 20 °C under the laser power density of 2.0 W cm^{-2}. This study showed that this system has excellent imaging ability and synergistic chemothermal therapy effect. A versatile synergistic therapy system such as DOX@UCNP@mSiO$_2$–AuNRs is expected to have wide biomedical applications and may be particularly useful for synergistic tumor therapy.

Introduction

With the development of nanotechnology, various delivery systems have been gradually constructed and have made significant contributions to the improvement of cancer diagnosis, imaging and therapy over the past few decades.[1–4] Among these systems, nanoparticle-based multifunctional delivery systems have attracted increasing attention owing to their excellent performance.[5–8] Smart combinations of different types of these multifunctional systems have been designed.[9] In these systems, various organic or inorganic nanomaterials, such as a lipid complex,[10] polymer,[11] silica,[12,13] gold[14] and TiO$_2$,[15] have been employed as the protective shells to construct the multifunctional systems by combining different inorganic nanomaterials as the cores (*e.g.* magnetic nanoparticles,[16] quantum

dots,[17] gold nanorods (AuNRs),[18] upconversion nanoparticles (UCNPs)[19]). For the shells, mesoporous silica is one of the best candidates because of its characteristics of large surface area, good biocompatibility and low cytotoxicity.[20,21] The stabilized structure of silica can not only protect the cores from external damage (*e.g.* acid), but also decrease the cytotoxicity of these cores.[22] Moreover, the large mesoporous channels can store the drug before their release, effectively avoiding the side effects to the normal tissue.[23] With these attractive features, more and more researchers have selected mesoporous silica as the shells to construct diverse systems, especially for those systems which have the imaging cores.[24,25]

It is well known that an outstanding imaging core often possess the deep tissue penetration, good photostability and relatively high brightness.[26,27] Therefore, nanoparticles which have these properties are usually acting as the imaging cores to construct the multifunctional system.[28] In these reported imaging cores, UCNPs have obtained great attention owing to their excellent optical properties.[29] The abilities of photon upconversion can let UCNPs sequentially absorb two or more near-infrared (NIR) photons and subsequently emit a single highenergy photon at the shorter wavelength, not only decreasing the phototoxicity and autofluorescence background, but also improving the tissue penetration depth.[30,31] However, most of these developed multifunctional systems are

State Key Laboratory of Chemo/Biosensing and Chemometrics, College of Biology, College of Chemistry and Chemical Engineering, Key Laboratory for Bio-Nanotechnology and Molecular Engineering of Hunan Province, Hunan University, Changsha 410082, P. R. China. E-mail: kmwang@hnu.edu.cn; xiaoxiaohe@hnu.edu.cn; Fax: +86 731 88821566; Tel: +86 731 88821566

† Electronic supplementary information (ESI) available: TEM images, hydrodynamic size, XRD, TEM-associated EDX spectra, fluorescence spectra, standard curve of DOX, MTT assay and related parameters of different nanoparticles. See DOI: 10.1039/c6ra27802g

‡ These authors contributed equally.

single-model therapy and imaging.[32,33] The use of systems which have functions of multi-model therapy and imaging are still in the early stages of research. Within this context, the systems with imaging and multi-model cancer therapy functions are being widely investigated, especially for the system which has combined the chemotherapy of antitumor drugs and photothermal therapy of plasmonic nanomaterials.[34,35] The combination of this two-model therapy (namely chemothermal cancer therapy) can then lead to the synergistic therapy effect that is better than the respective monotherapy from *vitro* to *vivo*.

Recently, various photothermal nanomaterials, such as magnetic nanoparticles,[36] cupelric sulfide nanoparticles,[37] palladium nanosheets[38] and gold nanomaterials,[39,40] have been widely used for chemothermal cancer therapy. Among these photothermal nanomaterials, AuNRs have achieved more attention due to their unique properties, such as easy synthesis, chemical inertness and excellent surface plasmon resonance (SPR) absorption.[41,42] The effective photosensitivity can give AuNRs the ability to absorb near-infrared (NIR) light, and the absorbed photon energy can be then converted into heat and dissipated to surroundings, leading to the increase of cell membrane permeability and subsequently destruction of biological samples.[43,44] Up to now, AuNRs-based chemothermal therapy systems are mainly core–shell structures. In these systems, mesoporous silica is usually acting as the shell to coat on the cores of AuNRs.[45,46] This structure not only guarantees a high drug payload, but also realizes the photothermal synergistic therapy of AuNRs.[47] For example, Ju *et al.* have reported a mesoporous silica-encapsulated AuNRs drug delivery system for mitochondria-targeted chemothermal therapy.[48] Nevertheless, a large number of these reported systems have usually encapsulated AuNRs into mesoporous silica shells, which have limited their design on the imaging function. According to these issues, developing a multifunctional delivery system, which combining chemothermal therapy and tumor imaging, is in an urgent demand.

Therefore, we here have sought to take advantage of these unique features of mesoporous silica, UCNPs and AuNRs to rationally design a core/satellite-like multifunctional drug delivery system for synergistic chemothermal therapy and tumor imaging. The schematic is illustrated in Fig. 1. In this work, UCNPs are first synthesized by the classic high-temperature solvent method. The as-synthesized UCNPs, selected as the imaging cores, are coated with a layer of mesoporous silica to form the core–shell nanomaterials (UCNP@mSiO$_2$). Subsequently, an antitumor drug of doxorubicin (DOX) has loaded into the pores to get DOX-loaded UCNP@mSiO$_2$ (DOX@UCNP@mSiO$_2$). In order to further achieve the abilities of drug controlled release and synergistic therapy, the positively charged AuNRs are subsequently employed as the satellite-like gatekeeper to block the pores of negatively charged mesoporous silica shell through the electrostatic interaction. Then, this multifunctional drug delivery system of AuNRs capped DOX@UCNP@mSiO$_2$ (DOX@UCNP@mSiO$_2$–AuNRs) has finally obtained. Under neutral condition (pH 7.0), the AuNRs can steadily attach to the surface of DOX@UCNP@mSiO$_2$, thus blocking the pores and limiting the release of loaded DOX. However, under acid condition (pH 4.9), the charge of mesoporous
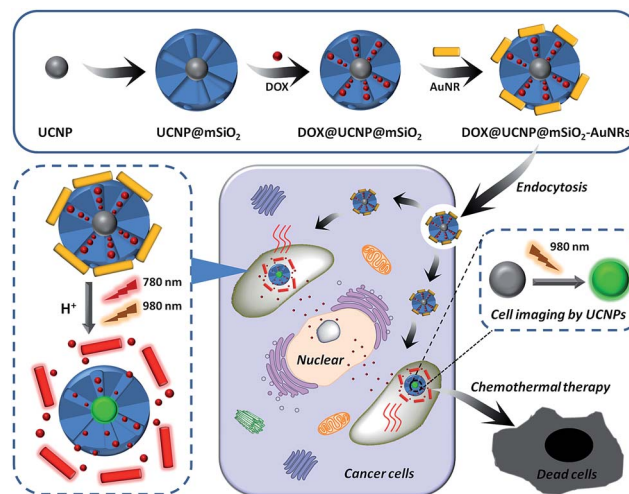

Fig. 1 Schematic illustration of the synthesis of satellite-like AuNRs capped mesoporous silica nano-container with UCNP cores and their application in intracellular synergistic chemothermal therapy and imaging under the stimuli of acidic condition (pH ~ 5) and laser irradiation (780 nm and 980 nm respectively).

silica has increased by the surface protonation and the AuNRs has subsequently separated, resulting in the release of entrapped DOX. Moreover, owing to the SPR property, the present AuNRs can effectively convert the NIR light into heat, which has gave DOX@UCNP@mSiO$_2$–AuNRs the chance to achieve the tumor photothermal therapy. The *in vitro* studies showed that this system has an excellent synergistic therapy and imaging abilities under the irradiation of 780 nm and 980 nm respectively. And this imaging under 980 nm can also obtained *in vivo*. Combining with these capabilities, we believe that this multifunctional system, which displayed two functions of synergistic therapy and imaging, will improve the development of nanocarrier and biomedical applications in cancer therapy.

Experimental section

Materials

Doxorubicin hydrochloride (DOX), hexahydrated yttrium (YCl$_3$·6H$_2$O), hexahydrated ytterbium (YbCl$_3$·6H$_2$O), Hexahydrated erbium (ErCl$_3$·6H$_2$O), auric chloride acid (AuCl$_4$), 4′,6-diamidino-2-phenylindole (DAPI), 3-[4,5-dimethylthialzol-2-yl]-2,5-diphenyl-tetrazolium bromide (MTT) and octadecene (ODE) were purchased from Sigma-Aldrich. Chloroform (CHCl$_3$) and cyclohexane were obtained from Shanghai Chemical Reagent Company (Shanghai, China). Hydrogen fluoride (NH$_4$F), tetraethylorthosilicate (TEOS, ≥28%) and sodium hydroxide (NaOH) were purchased from Sinopharm Chemical Reagent Co., Ltd (Shanghai China). Oleic acid (OA) was purchased from Fuyu Fine Chemicals Co., Ltd (Tianjing, China). *N*-Cetyltrimethylammonium bromide (CTAB, ≥99%) was obtained from Alfa Aesar (Tianjing, China). Absolute ethanol and absolute methanol were purchased from Anhui Ante Biochemical Co., Ltd (Suzhou, China). Other reagents and solvents were provided by Dingguo Reagent Company (Beijing,

China). All the chemical reagents in this experiment were analytical grade and used without further purification. All solutions were prepared and diluted using ultrapure water (18.2 MΩ cm) from the Millipore Milli-Q system (Barnstead Thermolyne NANO-pure, Dubuque, 1 A). Male athymic BALB/c (Balb/ C-nu) mice were purchased from Hunan SJA Laboratory Animal Co., Ltd. They were 4–6 weeks old at the start of each experiment and weighed 20–25 g. All animal operations were in accord with institutional animal use and care regulations, according to protocol No. SCXK (Xiang) 2013-0004, approved by the Laboratory Animal Center of Hunan Province.

Characterization

Transmission electron microscopy (TEM) images were taken using a F20 microscope with an accelerating voltage of 100 kV. The fluorescence spectra were measured on a Hitachi F-4500 FL Spectraphotometer. The UV-vis spectra were recorded by using a Beckman UV-vis Spectraphotometer. Small angle powder X-ray diffraction (XRD) pattern was obtained in a Scintag XDS-2000 powder diffractometer using CuKα irradiation ($\lambda = 0.154$ nm). N_2 adsorption–desorption isotherm was obtained at 77 K on a Micromeritics ASAP 2010 sorptometer by static adsorption procedures. Samples were degassed at 373 K and 10^{-3} Torr for a minimum of 12 h prior to analysis. Brunauer–Emmett–Teller (BET) surface area was calculated from the linear part of the BET plot according to IUPAC recommendations. Pore size distribution was estimated from the adsorption branch of the isotherm by the Barrett–Joyner–Halenda (BJH) method. The hydrodynamics diameters and zeta potentials were measured by using a Malvern ZetaSizer Nano instrument, equipped with a He–Ne laser (633 nm) at a fixed scattering angle of 90°. The Confocal laser scanning microscopy (CLSM) images were obtained on a Flouview FV4500, Olympus. The MTT assay was measured on a multimode reader M1000 (TECAN). The images of tumor were observed by using whole-body fluorescent imaging system.

Synthesis of UCNP

$YCl_3 \cdot 6H_2O$ (236.6 mg, 0.78 mmol), $YbCl_3 \cdot 6H_2O$ (77.5 mg, 0.2 mmol) and $ErCl_3 \cdot 6H_2O$ (7.6 mg, 0.02 mmol) were added into a 250 mL round-bottom flask. Then 2 mL of absolute methanol was added to form the uniform and clear solution. Subsequently, 6 mL of OA and 15 mL of ODE were added into the above solution. The obtain solution was vigorously stirred at room temperature for 1 h. In order to remove water vapour and methanol, the solution, which was protected by nitrogen, was then processed at vacuum (120 °C) for 10 min. After that, this solution was continue heated to 160 °C and stirred for 1 h to form a uniform and transparent yellow solution. Then this obtained yellow solution was cooled down to room temperature under the protection of nitrogen.

To finally obtain the UCNP, NH_4F (148.2 mg, 4 mmol) and NaOH (100 mg, 25 mmol) were dissolved in 10 mL absolute methanol to form a completely transparent solution via ultrasonic treatment. Then this transparent solution was dropwise added into the above yellow solution. After stirring for 2 h, this mixture was then heated to 120 °C for 30 minutes to remove the water vapour and methanol (the samples were protected by nitrogen in the vacuum condition). Then the solution was heated to 320 °C and reacted for 1.5 h under the protection of nitrogen. After cooling down to room temperature, 20 mL of ethanol was added into the mixture. The obtained products were collected by centrifugation (10 000 rpm, 10 min) and dispersed into 5 mL of cyclohexane. Then the products were further precipitated in 15 mL ethanol and finally dispersed into 3 mL of chloroform to achieve the OA coated UCNP. In order to show the successful synthesis of UCNP, the TEM images and Fourier transform infrared (FTIR) spectra was then carried out. The TEM images were taken using a F20 microscope with an accelerating voltage of 100 kV. In addition, the related properties of UCNP were characterized by the fluorescence spectra, hydrodynamics diameters and zeta potentials.

Synthesis of UCNP@mSiO₂

5 mg of CTAB was first dissolved into 5 mL of ultrapure water. Then this solution of CTAB was added into 1 mL of UCNP solution. After stirring for 30 min, the solution was heated to 70 °C. Then 5 μL of NaOH (2 M) and 100 μL of TEOS were added into the above solution for another 3 h reaction. Subsequently, the obtain mesoporous silica coated UCNP (UCNP@mSiO₂) nanoparticles were washed with ethanol and ultrapure water for three times and then stored in 1 mL of ultrapure water.

In order to remove the template of CTAB, 58 mg of as-prepared UCNP@mSiO₂ was dispersed in 15 mL ethanol which containing 150 μL HCl (37.2%). After reflux condensation for 16 h at 85 °C, the products were collected by centrifugation and washed with ethanol and ultrapure water for three times. Finally, the obtained UCNP@mSiO₂ was dried under high vacuum container at −60 °C. The TEM images were obtained in a F20 microscope with an accelerating voltage of 100 kV. The small angle powder X-ray diffraction (XRD) pattern achieved from a Scintag XDS-2000 powder diffractometer and the N_2 adsorption–desorption isotherm achieved from a Micromeritics ASAP 2010 sorptometer were used to show the structure of as-synthesized UCNP@mSiO₂. The fluorescence spectra and FTIR spectra of as-synthesized UCNP@mSiO₂ were respectively measured by the fluorescence spectraphotometer ($E_x = 980$ nm) and FTIR spectrometer. Moreover, the zeta potentials and hydrodynamics diameters of UCNP@mSiO₂ were measured by a Malvern ZetaSizer Nano instrument.

AuNRs synthesis and capping

The synthesis of gold nanorods (AuNRs) was based on the seed growth method. The procedures were listed as follow: $HAuCl_4$ (340 μL, 1%) and CTAB (5 mL, 0.4 M) were added to 2.4 mL ultrapure water under stirring. Then silver nitrate (2 mL, 1 mM) and ascorbic acid (200 μL, 0.1 M) were added into this solution. After mixing the solution to colourless, $NaBH_4$ (200 μL, 1 mM) was subsequently added. Then this solution was stirred for 10 min to form a dark brown mixture and standard for 5 min to finally obtain the AuNRs. The as-synthesized AuNRs was collected by centrifugation (12 000 rpm, 5 min) and washed with ultrapure water to remove the excess CTAB. The obtained

AuNRs were characterized by the TEM images and UV-vis spectra. In addition, the zeta potentials and hydrodynamics diameters of AuNRs were measured on the Malvern ZetaSizer Nano instrument.

Before capping with AuNRs, the antitumor drug of DOX was first loaded into the UCNP@mSiO$_2$ to get DOX@UCNP@mSiO$_2$. 1 mg of previously synthesized UCNP@mSiO$_2$ nanoparticles were dispersed into 1 mL ultrapure water which containing 1 mg of DOX. Then the solution was shook overnight to obtain DOX@UCNP@mSiO$_2$. Subsequently, AuNRs with different volume (0 μL, 50 μL, 250 μL, and 500 μL) were respectively added to the DOX@UCNP@mSiO$_2$ and dispersed by ultrasound. After shaking overnight, the result DOX@UCNP@mSiO$_2$–AuNRs were collected by centrifugation (10 000 rpm, 5 min) and washed several times until the supernatant became colourless. Then the DOX@UCNP@mSiO$_2$–AuNRs was finally obtained. All the supernatants were collected and measured by the UV-vis spectrophotometer. According to the difference in the amount of the initial and left DOX, the loading amount of DOX in DOX@UCNP@mSiO$_2$–AuNRs was calculated to be about 85.3 μmol g^{-1} SiO$_2$. The TEM images of DOX@UCNP@mSiO$_2$–AuNRs were obtained in a F20 microscope. And the UV-vis absorption spectrum of UCNP@mSiO$_2$ and DOX@UCNP@mSiO$_2$–AuNRs was respectively measured by the UV-vis spectrophotometer.

The capping feasibility and effect of AuNRs

The zeta potential of AuNRs and UCNP@mSiO$_2$ under different pH was first investigated to confirm the feasibility of capping of AuNRs. AuNRs and UCNP@mSiO$_2$ were respectively dispersed into PBS under different pH range from 4.0 to 8.0. Then the samples were measured via the Malvern ZetaSizer Nano instrument to obtain the zeta potentials of AuNRs and UCNP@mSiO$_2$ under different pH. Another experiment was also carried out to study the blocking effect of AuNRs. The above obtained DOX@UCNP@mSiO$_2$–AuNRs (0.3 mg) which have synthesized with different concentration of AuNRs were respectively added into a cuvette. Then 200 μL of PBS (pH 7.0) was carefully filled into this cuvette. The fluorescence intensity of released DOX was monitored every 1 h.

Stimulus-response behavior of DOX@UCNP@mSiO$_2$–AuNRs

The uncapping ability of AuNRs at acid condition was first investigated. 1.0 mg of DOX@UCNP@mSiO$_2$–AuNRs was respectively dispersed into 500 μL different media (1 M: NaCl, KCl, ZnCl$_2$, Na$_2$SO$_4$, lactose, glucose, glycine, BAS, PBS: pH 7.0 and PBS: pH 5.0). After incubating the samples for 9 h, the suspensions of these samples were collected by centrifugation and subsequently measured by a fluorescence spectrophotometer to get the fluorescence intensity of released DOX. Then the release behavior of DOX from DOX@UCNP@mSiO$_2$–AuNRs under different pH was further investigated. 0.3 mg of DOX@UCNP@mSiO$_2$–AuNRs was respectively added into 200 μL PBS buffer under different pH (7.4, 6.5, 4.9, 2.0). Then the supernatants of these samples was collected every 1 h for nine times through centrifugation. Finally, NaOH solution was used to destroy the structure of this system to release all of

loaded DOX and the released percentage of DOX from DOX@UCNP@mSiO$_2$–AuNRs can be calculated. The DOX released to the supernatant was monitored by the F-4500 fluorescence spectrophotometer ($\lambda_{ex} = 480$ nm, $\lambda_{em} = 560$ nm). % released percentage = (released amount in every 1 h)/(total loading amount).

Photothermal performance of DOX@UCNP@mSiO$_2$–AuNRs

The photothermal effect of DOX@UCNP@mSiO$_2$–AuNRs under different laser power density was first investigated. 1 mg of DOX@UCNP@mSiO$_2$–AuNRs was dispersed in 1 mL PBS buffer (pH 7.0). Then the sample was irradiated with NIR laser for 27 min and the temperature of sample was measured every 1 min. Here, five samples were respectively irradiated with NIR laser under different power density (780 nm at 0, 1.0, 1.5, 2.0, 2.5 W cm^{-2}). Another experiment was also carried out to study the photothermal effect of DOX@UCNP@mSiO$_2$–AuNRs under different samples concentrations. Samples with the final concentrations of 100, 400, 800, 1000 μg mL^{-1} were irradiated with NIR laser (780 nm, 2.0 W cm^{-2}) for 27 min. The temperature of samples were also measured every 1 min. In addition, the effect of AuNRs on the release of DOX under NIR irradiation was researched. 1 mg of DOX@UCNP@mSiO$_2$–AuNRs was dispersed in 1 mL PBS buffer under different pH (4.9 and 7.4). After standing for 3 h, the supernatants of these samples were collected by centrifugation. For another two groups, the samples which containing 1 mg mL^{-1} DOX@UCNP@mSiO$_2$–AuNRs under different pH (4.9 and 7.4) was first irradiated by the NIR laser for 27 min. Subsequently, the samples were also standard for 4 h and the supernatants were then collected. The collected supernatants were measured by the F-4500 fluorescence spectrophotometer to obtain the fluorescence intensity of released DOX.

The confocal laser scanning microscope (CLSM) imaging

SMMC-7721 cells were seeded into 35 mm plastic-bottomed u-dishes and cultured in RPMI-1640 medium which contained 10% FBS. Then the cells were incubated in a humidified 5% CO$_2$ atmosphere at 37 °C for 12 h. After that, the cells were treated with DOX@UCNP@mSiO$_2$–AuNRs (100 μg mL^{-1}) at 37 °C for 6 h and 24 h respectively. After treatment, the medium was removed and the cells were washed twice with D-hanks. Subsequently, 1 μL of DAPI was added into cells to stain the cell nucleus. After 15 min treatment, the cells were washed with PBS buffer and imaged by CLSM (100× oil-immersion objective).

Cytotoxicity assays

The cytotoxicity of nanoparticles was investigated by the MTT assays. SMMC-7721 cells were seeded into 96-well plates at a density of 7×10^3 cells per well. Then the cells were incubated at 37 °C and 5% CO$_2$ for 12 h. Subsequently, the cells were respectively treated with UCNP@mSiO$_2$–AuNRs, DOX@UCNP@mSiO$_2$–AuNRs and free DOX for 48 h under different concentration range from 2.562 to 200 μg mL^{-1}. Another 96-well plate, which was also added into UCNP@mSiO$_2$–AuNRs, DOX@UCNP@mSiO$_2$–AuNRs and free DOX, was then carried out. After incubating cells with

different samples for 24 h, the cells were further irradiated with NIR laser for 10 min. After that, the cells were incubated for another 24 h. Finally, all of supernatants in 96-well plate were removed and the cells were incubated with 180 μL medium and 20 μL MTT (0.5 mg mL^{-1}) for 4 h. After removing the medium carefully, DMSO (150 μL) was added into each well. All wells were shook at 37 °C for 10 minutes and the optical density (OD) was measured at 490 nm using a multi-detection microplate reader. The OD was measured to calculate the cell viability. The cell viability = $(OD_{treated}/OD_{control}) \times 100\%$.

In vivo fluorescence imaging

Athymic BALB c male mice were purchased from the Shanghai SLAC Laboratory Animal CO., Ltd. and maintained under pathogen-free conditions. All animals operations were in accord to the protocol No. SYXK (Xiang) 2008-0001, approved by the Laboratory Animal center of Hunan. The tumor model was established by subcutaneous injection of 200 μL of SMMC-7721 cells suspension solution (5×10^7 per cells) into the right fore limb. A solid tumor with the diameter of 0.5 cm was formed after 3 weeks. The healthy mice were randomly divided into two groups ($n = 3$). After anesthetizing by isoflurane gas, 200 μL of UCNP@mSiO$_2$ solution was directly injected into the tumor site of the tumor bearing mice and the abdominal cavity of healthy mice respectively. For the control, equivalent physiological saline was injected into the other group of healthy mice by tail intravenous injection. Bioluminescence images were obtained using an IVIS Imaging System (Xenogen). The excitation wavelength of assay group and control group was 980 nm and 465 nm respectively. The acquisition time was 60 s.

Results and discussion

Synthesis and characterization of UCNP@mSiO$_2$

In order to obtain the core/satellite-like multifunctional system with the functions of chemothermal synergistic therapy and tumor imaging, the DOX@UCNP@mSiO$_2$–AuNRs nanocarrier described above was first synthesized. In this system, three components, which have named the solid supporter shell, the satellite-like cap with photothermal function and the imaging core, were respectively employed. As the suitable imaging material with excellent optical properties, UCNPs have been selected as the imaging core and subsequently synthesized by the classic high-temperature solvent method. The as-prepared UCNPs were characterized by transmission electron microscopy (TEM), dynamic light scattering (DLS) and fluorescence spectra respectively. TEM images (Fig. 2A and S1A†) showed that the UCNPs have a uniform size of ∼20 nm, which has corresponded to the measured result of DLS in Table S2† (∼23 nm). The small size of UCNPs can limit the size of final nanoparticles after coating with mesoporous silica shells, effectively increasing the cellular uptake of final system. The similar system with small size of UCNPs was also reported in Shi's work.[49] The fluorescence spectra (Fig. 3D) displayed that the synthesized UCNPs have the two characteristic emission peaks ($E_x = 980$ nm) at 550 nm (the strong peak) and 660 nm (the weak
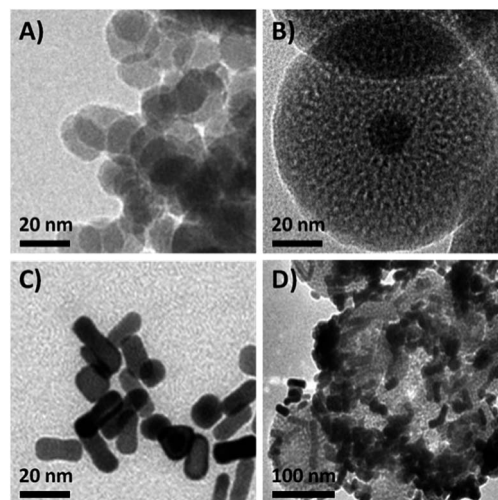

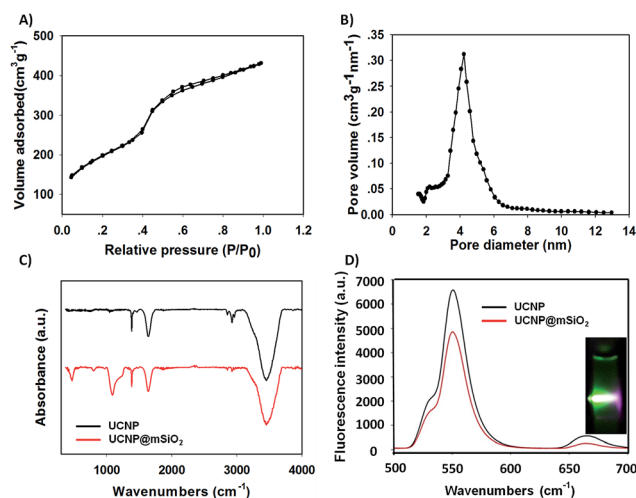**Fig. 2** TEM images of UCNPs (A), UCNP@mSiO$_2$ (B), AuNRs (C) and DOX@UCNP@mSiO$_2$–AuNRs (D).

Fig. 3 Nitrogen sorption isotherms (A) and pore size distribution plots (B) of UCNP@mSiO$_2$, FTIR spectra (C) and fluorescence spectra (D) of UCNPs and UCNP@mSiO$_2$. Inset: the fluorescence image of UCNPs under excitation of 980 nm (D).

peak), which have corresponded to the fluorescence spectra of reported UCNPs (e.g. Shi's work[49]). This result demonstrated that the as-synthesized UCNPs might have the ability of tumor imaging at the NIR irradiation of 980 nm. Subsequently, the mesoporous silica layer, acted as the solid supporter shell, was then coated on the UCNPs via the sol–gel method. The TEM images were first illustrated this coating behaviour of mesoporous silica and the typical core–shell structure of UCNP@mSiO$_2$. As showed in Fig. 2B and S1B,† the obtained UCNP was coated with a bright layer of amorphous mesoporous silica, and the thickness of this layer was about ∼45 nm. Compared with other system (23 nm),[50] the mesoporous silica shell in our work has a little thick. The thick shell has increased the size of our nanoparticles, but it did not affect the function of this system due to the small core of UCNP and the appropriate

size of UCNP@mSiO$_2$. In addition, owing to this thick shell, the UCNP@mSiO$_2$ might have the higher drug loading ability, which can subsequently increase the chemotherapy effect of this system. The DLS assay disclosed that the hydrodynamic size (Fig. S1C and Table S2†) of obtained UCNP@mSiO$_2$ was ~120 nm, which was similar to the size observed in TEM image (Fig. 2B).

In addition, the change of element composition of different samples (from UCNPs to UCNP@mSiO$_2$) during the coating process was also proofed through the TEM-associated energy-dispersive X-ray spectroscopy (EDS). It was displayed in Fig. S2,† the element composition of UCNP was O, F, Na, Er, Cl, Y and Yb. However, after coating with mesoporous silica layer, the element of Si has appeared in the element composition of UCNP@mSiO$_2$. This appeared element of Si was belonged to the mesoporous silica layer. The distinction of element composition between UCNPs and UCNP@mSiO$_2$ has provided the anticipated evidence to the coating behaviour of mesoporous silica layer. In addition, the Fourier transform infrared (FTIR) spectra was also confirmed this coating process (Fig. 3C). Compared with the characteristic absorption bands of UCNPs, the two new absorption bands, which located around 800 cm^{-1} and 1080 cm^{-1}, have appeared in the characteristic absorption bands of UCNP@mSiO$_2$. The appeared two new absorption bands were attributed to the stretching vibration of silicon–oxygen bond. This result has again verified that the mesoporous silica layer was indeed covered on the surface of UCNP.

After proving the successful coating of mesoporous silica, the as-obtained UCNP@mSiO$_2$ was further characterized by small-angle X-ray diffraction (XRD), N$_2$ adsorption–desorption isotherms and fluorescence spectra to investigate the structure and fluorescence properties of UCNP@mSiO$_2$. As illustrated in Fig. S3,† six significant small-angles XRD peaks were appeared in the $10° > 2\theta > 80°$ range. In these peaks, the Bragg peaks of {100}, {110}, {200} were the typical XRD peaks of MCM-41-type mesoporous material, and the {111}, {220}, {311} Bragg peaks were the typical XRD peaks of β-NaYF4 crystal which has a hexagonal structure. These results of XRD characterization were similar to the result in Shi's work,[49] which also has the same small-angles XRD peaks of UCNPs. Moreover, the N$_2$ adsorption–desorption isotherm was also confirmed this typical MCM-41-type structure of mesoporous silica shell. In Fig. 3A, the UCNP@mSiO$_2$ showed a strong, sharp, and single adsorption step in the relative pressure around 0.4, which was belonged to the adsorption step of MCM-41-type mesoporous structure. In addition, by using BET and BJH model, the specific surface area, the pore distribution and the average pore diameter of UCNP@mSiO$_2$ were finally obtained. As showed in Fig. 3B and Table S1,† the UCNP@mSiO$_2$ displayed a narrow pore distribution. And the average pore diameter of UCNP@mSiO$_2$ was about 4.2 nm, which was bigger than that of other nanoparticle systems (usually 2–3 nm (ref. 50)). This result suggested that the system of UCNP@mSiO$_2$ can easily load drugs and the release of these loaded drugs can also achieve easily. Moreover, the specific surface area and pore volume of UCNP@mSiO$_2$ was 211.3 m^2 g^{-1} and 0.236 cm^3 g^{-1} respectively. The big pore volume and surface area have made UCNP@mSiO$_2$

easier to load drugs and construct the final system. As a multifunctional drug delivery system with the imaging function, it was necessary to further investigate the fluorescence properties of this system. A modified F-4500 fluorescence spectrometry was used to measure the fluorescence properties of UCNP and UCNP@mSiO$_2$ at the same concentration ($E_x = 980$ nm). The results were illustrated in Fig. 3D. Compared with UCNP, the emission peaks of UCNP@mSiO$_2$ have not changed on the position. And the intensity of these emission peaks has still kept strong. This result proved that the coating behaviour of mesoporous silica has not affected the optical properties of UCNP. The nanoparticle of UCNP@mSiO$_2$ can also realize the function of tumor imaging. According to the results described above, the excellent system of UCNP@mSiO$_2$ which has the potential functions of drug delivery and tumor imaging was obtained.

AuNR capping and detaching

To further obtain the stimuli-responsive drug delivery system, the satellite-like AuNRs were subsequently synthesized via the seed-mediated growth method. The as-synthesized AuNRs were directly confirmed by TEM images. As illustrated in Fig. 2C, the as-synthesized AuNRs have showed the uniform and well-defined rod like nanostructures. The average aspect ratio of these AuNRs was calculated to be about 3.0 (Table S2†). The appropriate size and the good dispersibility have given AuNRs the potential to assemble with UCNP@mSiO$_2$ for the final system. The UV-vis absorption spectrum in Fig. 4A showed that the AuNRs have the maximum absorption at 780 nm. This result has confirmed that the as-synthesized AuNRs might have the ability to convert the NIR light into heat and then trigger the tumor photothermal therapy. Subsequently, in order to investigate whether the AuNRs can attach to UCNP@mSiO$_2$ by the electrostatic interactions and then separate from UCNP@mSiO$_2$ under low pH, the zeta potentials of AuNRs and UCNP@mSiO$_2$
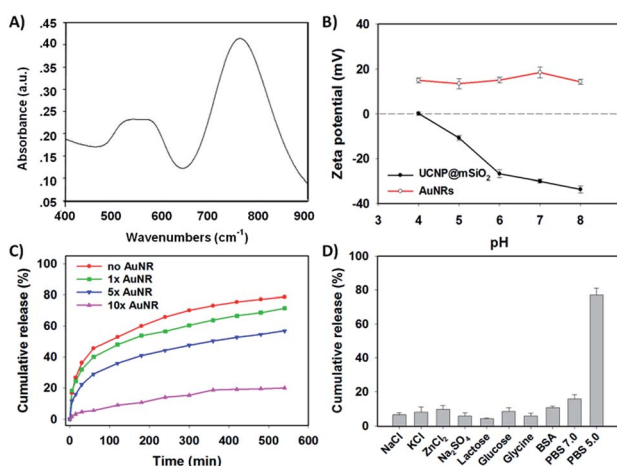

Fig. 4 (A) UV-vis absorption spectrum of AuNRs. (B) Zeta potential of AuNRs and UCNP@mSiO$_2$. (C) Cumulative release curve of DOX from DOX@UCNP@mSiO$_2$–AuNRs under different adding amount of AuNRs cap (1× = 50 μL, 2× = 250 μL, 10× = 500 μL, pH 7.0). (D) Cumulative release curve of DOX from DOX@UCNP@mSiO$_2$–AuNRs under different conditions (0.1 M each).

under different pH have been further measured. As showed in Fig. 4B, the zeta potential of AuNRs has not changed under different pH range from 4.0 to 8.0. And these zeta potentials of AuNRs have kept around 15 mV. However, in the same pH range, the zeta potentials of UCNP@mSiO$_2$ have got the large change. With the decreased pH, the zeta potential of UCNP@mSiO$_2$ has gradually increased. The zeta potential of UCNP@mSiO$_2$ under pH 4.0, 5.0, 6.0, 7.0 and 8.0 was about 0.15, -10.8, -26.8, -30.0, -33.6 mV respectively. This gradually increased zeta potential was mainly attributed to the surface protonation of UCNP@mSiO$_2$. The change of zeta potential in AuNRs and UCNP@mSiO$_2$ under different pH has given AuNRs the possibility to block the pores at neutral condition (pH 7.0) and separate from the UCNP@mSiO$_2$ at acid condition (pH < 6.0).

After investigating the possibility of capping and detaching of AuNRs, the capping feasibility and the effect of AuNRs under different concentrations were further studied. Here, the anti-tumor drug of DOX was selected as the model molecule to fabricate DOX-loaded UCNP@mSiO$_2$ (DOX@UCNP@mSiO$_2$). As illustrated in Fig. 4C, the DOX@UCNP@mSiO$_2$ without AuNRs treatment has an excellent release amount of DOX. This result was attributed to the unlocked pores of DOX@UCNP@mSiO$_2$. However, when incubating DOX@UCNP@mSiO$_2$ with AuNRs overnight, the released DOX has decreased to a certain extent. These results have demonstrated that the AuNRs can indeed attach to the surface of DOX@UCNP@mSiO$_2$ and then block the pores of mesoporous silica shell. In addition, with the increased concentration of AuNRs, the released DOX has gradually decreased. The percentage of released DOX can decrease to 18.9% after treating DOX@UCNP@mSiO$_2$ with 500 μL AuNRs. These results proved that the capping effect of AuNRs was concentration-dependent. When increasing the concentration of AuNRs, the blocking effect of AuNRs has also increased. According to the researches described above, we have finally selected 10× AuNRs to form the AuNRs-capped DOX@UCNP@mSiO$_2$ (DOX@UCNP@mSiO$_2$–AuNRs).

The TEM image has showed this finally obtained DOX@UCNP@mSiO$_2$–AuNRs. It can be seen from Fig. 2D, the AuNRs were attached to the surface of DOX@UCNP@mSiO$_2$. This result was the most direct evidence to proof the locking behaviour of AuNRs all around the DOX@UCNP@mSiO$_2$. Moreover, the UV-vis absorption spectrum of DOX@UCNP@mSiO$_2$–AuNRs has displayed two absorption peaks around 500 nm and 780 nm. These two absorption peaks were respectively belonged to the absorption peak of DOX and AuNRs. The result of UV-vis absorption spectrum in DOX@UCNP@mSiO$_2$–AuNRs has demonstrated that the capping behaviour of AuNRs has not affected the NIR absorption ability of AuNRs. The AuNRs absorbed on the surface of DOX@UCNP@mSiO$_2$ also have the ability of photothermal conversion. As we know, the zeta potential of UCNP@mSiO$_2$ has increased under the acid condition (pH < 6.0). Therefore, in order to clearly demonstrate that the AuNRs can separate from the surface of UCNP@mSiO$_2$ under acid condition, a specifically responsive experiment under different conditions was subsequently carried out. In this research, the DOX@UCNP@mSiO$_2$–AuNRs was respectively treated with

different samples for 5 h. As showed in Fig. 4D, only PBS (pH 5.0) triggered an increased release of loaded DOX, whereas no obvious release of DOX was observed in the presence of other samples. The excellent release of DOX in PBS (pH 5.0) was mainly attributed to the change of zeta potential on the surface of DOX@UCNP@mSiO$_2$, which has subsequently caused the separation of absorbed AuNRs and the opened pores. According to these results, the system of DOX@UCNP@mSiO$_2$–AuNRs which has the good pH-responsive ability was obtained.

Controlled release behaviour and photothermal effect of DOX@UCNP@mSiO$_2$–AuNRs

After confirming the capping and detaching behaviour of AuNRs, the controlled release of DOX from DOX@UCNP@mSiO$_2$–AuNRs under different pH was then investigated. By monitoring with fluorescence emission spectroscopy at 560 nm ($E_x = 480$ nm), the percentage of released DOX was finally obtained *via* the reference of standard curve from DOX (Fig. S6†). Fig. 5A showed that the release of DOX from DOX@UCNP@mSiO$_2$–AuNRs was pH- and time- dependent. With the decreased pH, the release amount of DOX has gradually increased. This result was attributed to the separation of AuNRs through the surface protonation of DOX@UCNP@mSiO$_2$–AuNRs. Moreover, under the acid condition of pH 4.9, the percentage of released DOX has reached 65% within 600 min. This result has suggested that the system of DOX@UCNP@mSiO$_2$–AuNRs might have the same released effect of DOX in cancer cells which have the similar acid condition (pH ∼ 5.0) in lysosome. Another experiment has been taken to investigate the effect of AuNRs on the release of DOX under NIR irradiation. As illustrated in Fig. S4,† after NIR irradiating, the fluorescence intensity of released DOX has a little increase both under pH 4.9 and pH 7.4. This phenomenon mainly attributed to the photothermal conversion of AuNRs, which has
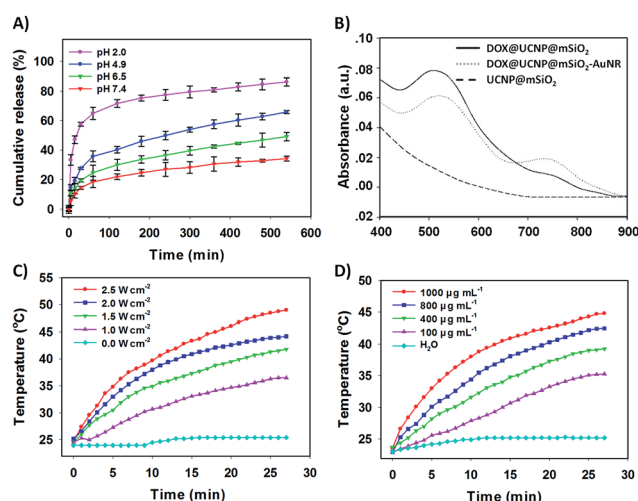

Fig. 5 (A) Controlled release curves of DOX@UCNP@mSiO$_2$–AuNRs under different pH. (B) UV-vis absorption spectrum of different samples. (C) The photothermal effects of DOX@UCNP@mSiO$_2$–AuNRs (1 mg mL^{-1}) under different laser irradiation. (D) The photothermal effects of DOX@UCNP@mSiO$_2$–AuNRs under different concentration (the power density was 2.0 W cm^{-2}).

subsequently triggered the increased temperature of sample and the accelerated release of loaded DOX. The accelerated release of DOX under the NIR irradiation has suggested that the NIR light in this system not only can trigger the photothermal therapy of tumor, but also can improve the efficacy of chemotherapy.

To further study the photothermal conversion ability of DOX@UCNP@mSiO₂, the UV-vis absorption spectrum of different samples were first investigated. As illustrated in Fig. 5B, only DOX@UCNP@mSiO₂–AuNRs has showed the UV-vis absorption peak of DOX and AuNRs. The UCNP@mSiO₂ did not have the UV-vis absorption peak at the range from 400 nm to 900 nm and the DOX@UCNP@mSiO₂ only have the UV-vis absorption peak of DOX. These results have demonstrated that the components of DOX, UCNP and mesoporous silica have not affected the UV-vis absorption ability of AuNRs. This little effect of nanoparticle system on the UV-vis absorption ability of AuNRs also can be achieved in Kim's work.[50] It was worth noting that the UV-vis absorption peak of DOX from DOX@UCNP@mSiO₂–AuNRs has a little decrease and red shift. This result mainly attributed to the UV-vis absorption of AuNRs range from 500 nm to 600 nm (Fig. 4A). Subsequently, the effect of NIR light on the temperature change of DOX@UCNP@mSiO₂–AuNRs solution was further researched. Fig. 5C showed that the solution temperature of DOX@UCNP@mSiO₂–AuNRs was unchanged under the laser power density of 0 W cm⁻². However, when increasing the laser power density at 780 nm, the solution temperature has gradually increased. And the temperature can reach 36.5 °C, 41.8 °C, 44.2 °C and 49.0 °C after irradiating with different laser power density (1.0 W cm⁻², 1.5 W cm⁻², 2.0 W cm⁻² and 2.5 W cm⁻² respectively). These results have indicated that the system of DOX@UCNP@mSiO₂–AuNRs can efficiently convert the NIR light into heat, and this photothermal effect generated by the AuNRs has positively correlated with the laser power density. It has been reported that the temperature which was greater than 45 °C can induce the apoptosis via hyperthermia.[51] Therefore, in order to select the best laser power density of this system and decrease the damage of high temperature ($T \geq 45$ °C) to the surrounding normal tissues and cells, an assistant experiment about the effect of NIR light on the cell viability was subsequently carried out. It can be seen in Fig. S7,† most of cells were still survived after irradiating these cells with NIR light at the power density of 1.0, 1.5, 2.0 W cm⁻² respectively. However, only 79% of cells were survived under the laser power density of 2.5 W cm⁻². This result suggested that the NIR light at the power density of 2.5 W cm⁻² has a certain degree of cytotoxicity. According to these results, we have finally employed the laser power density of 2.0 W cm⁻², which can effectively convert NIR light into heat and has the low cytotoxicity, as the optimum laser power density for the following experiments.

Fig. 5D has displayed the change of temperature from the DOX@UCNP@mSiO₂–AuNRs solution under the different sample concentrations. With the increased sample concentrations of DOX@UCNP@mSiO₂–AuNRs, the temperature of solution has gradually increased after irradiating the sample for 30 min (780 nm, 2.0 W cm⁻²). Even at the concentration of 100 μg mL⁻¹, the temperature of solution has also increased 10 °C.

The change of temperature from DOX@UCNP@mSiO₂–AuNRs solution under different concentrations can further help us to determine the appropriate irradiation time and the sample concentrations in the specific experiments. For example, in order to open the double-strand structures of DNA valves ($T \geq 44$ °C) and decrease the chance of apoptosis by hyperthermia ($T \leq 45$ °C), an appropriate sample concentration of 800 μg mL⁻¹ with 27 min irradiation (780 nm, 2.0 W cm⁻²) can be selected.[52] From these findings described above, the excellent pH-responsive controlled release behaviour and the effectively photothermal conversion ability of DOX@UCNP@mSiO₂–AuNRs have been well displayed.

Intracellular controlled release and imaging

The above described features of DOX@UCNP@mSiO₂–AuNRs system have motivated us to further study the drug delivery behaviour and imaging intracellular. Prior to study the drug delivery behaviour and imaging of this system, the effect of AuNRs on the fluorescence spectra of UCNP was first investigated. As showed in Fig. S5,† by the irradiation of NIR light ($E_x = 980$ nm), the UCNPs displayed two strong fluorescence emission peaks at 550 nm and 660 nm. Especially at the laser power density of 1.5 W cm⁻², the fluorescence intensity of UCNPs at 550 nm has exceeded the detection range of fluorescence spectrophotometer. These results have confirmed that the as-synthesized UCNPs have a good optical property, and the fluorescence intensity of UCNPs was mainly depended on the laser power density. However, when adding AuNRs into the sample of UCNPs, the fluorescence emission peaks of UCNPs were decreased to a certain extent both under the power density of 1.0 W cm⁻² and 1.5 W cm⁻². This result was mainly attributed to the NIR light absorption of AuNRs at 980 nm. Although the fluorescence emission peaks of UCNPs have decreased in the present of AuNRs, the fluorescence intensity of UCNPs has still kept strong and it was also enough to image in cells. After investigating the effect of AuNRs on the optical property of UCNPs, the drug delivery behaviour and the intracellular imaging of DOX@UCNP@mSiO₂–AuNRs were subsequently researched. Herein, SMMC-7721 cells (human liver cancer cell lines) were employed as the model cell line to determine whether the DOX@UCNP@mSiO₂–AuNRs can internalize into cells for imaging and release the loaded DOX by the acid condition intracellular. The cells were imaged by the confocal laser scanning microscope (CLSM) and the special staining material of DAPI with blue fluorescence was employed as the indicator to stain the cell nucleus. As illustrated in Fig. 6, after incubating DOX@UCNP@mSiO₂–AuNRs with SMMC-7721 cells for 6 h, a low red fluorescence of DOX was observed in cells. This low fluorescence of DOX was mainly attributed to the self-quenching of unreleased DOX under high concentration and the quenching behaviour of attached AuNRs. However, when incubating SMMC-7721 cells with DOX@UCNP@mSiO₂–AuNRs for 24 h, a high red fluorescence of DOX was appeared in the cells. The surface protonation of mesoporous silica shell under the acid condition (e.g. pH ~ 5.0 in lysosome) and subsequently opened pores of this system were the main reasons for this
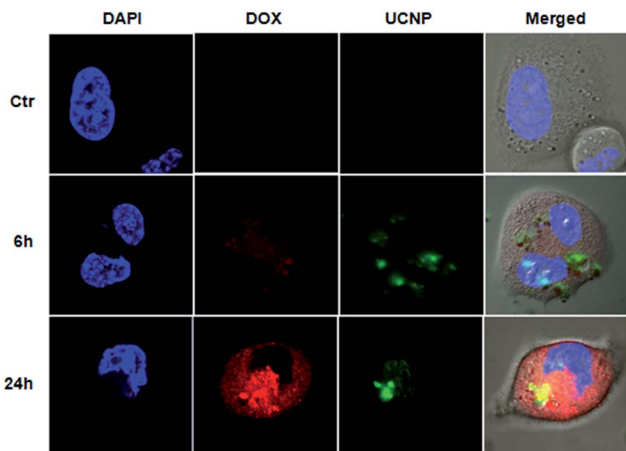
Fig. 6 CLSM image of the controlled release behaviors of DOX@UCNP@mSiO$_2$–AuNRs and the cell imaging of UCNPs after incubating DOX@UCNP@mSiO$_2$–AuNRs with SMCC-7721 cells for 6 h and 24 h respectively at the sample concentration of 100 μg mL^{-1}. The cell nucleus was stained by Blue-fluorescent DAPI. Cells were imaged by a 100× oil-immersion objective.
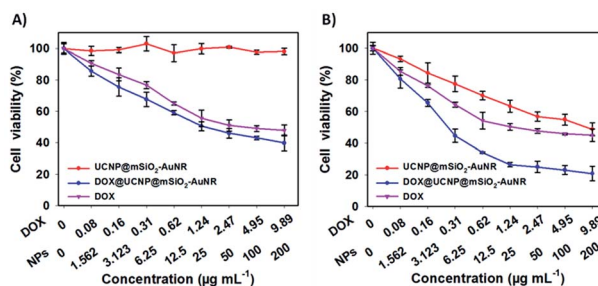

Fig. 7 The cytotoxicity assay curves for SMCC-7721 cells after treating with UCNP@mSiO$_2$–AuNRs, DOX@UCNP@mSiO$_2$–AuNRs and DOX respectively. (A) The cytotoxicity assay without NIR light irradiation. (B) The cytotoxicity assay under NIR light irradiation (the power density was 2 W cm^{-2}).

increased fluorescence of DOX. Moreover, owing to the increased distance between AuNRs and released DOX, the quenching effect of AuNRs to DOX has been weakened, which can also induce the increase of DOX fluorescence. As demonstrated above, this pH-responsive drug delivery system can be used to delivery drugs into cancer cells.

In addition, the cell imaging of DOX@UCNP@mSiO$_2$–AuNRs was also investigated. As we know, the UCNPs did not have the self-quenching phenomenon and the effect of AuNRs on the fluorescence spectra of UCNPs was small (Fig. S5†). Therefore, the DOX@UCNP@mSiO$_2$–AuNRs can keep a strong green fluorescence under the irradiation of NIR light at 980 nm in both two incubation time (6 h and 24 h). In contrast, neither red fluorescence nor green fluorescence was observed in control sample. This result has proved that the red fluorescence and the green fluorescence in cells were indeed belonged to the DOX and UCNPs respectively. All of these results have indicated that the system of DOX@UCNP@mSiO$_2$–AuNRs can internalize into cells and effectively deliver drugs to cells *via* the pH-triggered stimuli-responsive release behaviour intracellular. In addition, this system also has the excellent fluorescence imaging function, which can be then used to tumor imaging in cancer therapy.

Cytotoxicity assay

As the multifunctional system of DOX@UCNP@mSiO$_2$–AuNRs, it was necessary to further investigate the synergistic therapy effect of chemotherapy and photothermal therapy. The MTT assay was used to evaluate this synergistic therapy effect. As showed in Fig. 7A, without NIR irradiating, the UCNP@mSiO$_2$–AuNRs has displayed a negligible cytotoxicity to SMMC-7721 cells at the sample concentration range from 1.562 μg mL^{-1} to 200 μg mL^{-1}. This result has indicated that the UCNP@mSiO$_2$–AuNRs has the low cytotoxicity and the good

biocompatibility. However, the DOX@UCNP@mSiO$_2$–AuNRs has exhibited a certain degree of cytotoxicity, and this cytotoxicity was higher than that of free DOX. The high cytotoxicity of DOX@UCNP@mSiO$_2$–AuNRs was mainly attributed to the drug store ability of DOX@UCNP@mSiO$_2$–AuNRs before internalization and the excellent drug release behaviour of this system after endocytosis. The above results have demonstrated that the system of DOX@UCNP@mSiO$_2$–AuNRs can deliver more drugs into cells, which has increased the final therapeutic effect of this system. Another experiment was then carried out to further study the synergistic therapy effect of chemothermal therapy. It can be seen from Fig. 7B, after irradiating with NIR light (780 nm, 2.0 W cm^{-2}), the cytotoxicity of UCNP@mSiO$_2$–AuNRs was increased, which has presented a striking contrast to the cells that has not irradiated with NIR light (Fig. 7A). The good photothermal conversion property of AuNRs was the main reason for the cytotoxicity of UCNP@mSiO$_2$–AuNRs. Moreover, when loading DOX into UCNP@mSiO$_2$–AuNRs, the cytotoxicity of UCNP@mSiO$_2$–AuNRs was dramatically increased after irradiating cells with NIR light. The cell viability of SMMC-7721 cells was decreased to 20.7%. The increased cytotoxicity and the decreased cell viability were the directly evidence to prove the synergistic therapy ability of this system. All of these results have suggested that this multifunctional system has an excellent synergistic therapy ability of chemothermal therapy, and this system will promote the development of nanocarrier in the fields of drug delivery and tumor therapy.

Fluorescence imaging *in vivo*

The excellent cell imaging ability of DOX@UCNP@mSiO$_2$–AuNRs has motivated us to further investigate the tissue imaging of UCNP@mSiO$_2$–AuNRs *in vivo*. As displayed in Fig. 8A, with the excitation of visible light at 465 nm, the healthy nude mouse, which has injected with normal saline *via* tail intravenous injection, has showed the high autofluorescence. This autofluorescence of living tissues can largely affect the fluorescence imaging of most antitumor drugs owing to the similar fluorescent absorption bands of these drugs in visible light (*e.g.* antitumor drug of DOX). The large background signal of tissue autofluorescence can decrease the signal noise ratio of

Fig. 8 Fluorescence images of UCNP@mSiO$_2$–AuNRs *in vivo*: (A) fluorescence imaging of healthy nude mouse after tail intravenous injection of normal saline (E_x = 465 nm). (B) Fluorescence imaging of healthy nude mouse after Intraperitoneal injection of UCNP@mSiO$_2$–AuNRs (E_x = 980 nm). (C) Fluorescence imaging of SMMC-7721-tumor-bearing mice after injecting UCNP@mSiO$_2$–AuNRs in tumor site (E_x = 980 nm).

samples, significantly affecting the sensitivity and accuracy of tissue imaging. However, when employing UCNP@mSiO$_2$–AuNRs as the imaging tool to perform tissue imaging, the healthy nude mouse, which has injected with UCNP@mSiO$_2$–AuNRs through Intraperitoneal injection, has displayed a strong fluorescence at the injection site *via* the irradiation of NIR light at 980 nm (Fig. 8B). Using UCNP@mSiO$_2$–AuNRs as the imaging tool to obtain tissue imaging assay can not only effectively increase the signal noise ratio, accuracy and tissue penetration during imaging, but also can decrease the tissue damage triggered by laser. In addition, we also have used the system of UCNP@mSiO$_2$–AuNRs in tumor imaging. It can be seen in Fig. 8C, after injecting UCNP@mSiO$_2$–AuNRs into tumor site, a strong fluorescence signal of UCNPs has been subsequently observed in the tumor area of nude mouse. This result has confirmed that the system of UCNP@mSiO$_2$–AuNRs also can be used to the tumor imaging in cancer therapy.

Conclusions

In summary, we have successfully developed a core/satellite-like multifunctional drug delivery system for pH- and NIR- responsive chemothermal synergistic therapy and tumor imaging. The mechanisms behind pH- and NIR- response are the electrostatic interaction between AuNRs and mesoporous silica shells and the SPR absorption property of AuNRs. By irradiating with laser at 980 nm, the excellent tumor imaging, which can increase the signal noise ratio, accuracy and tissue penetration, has been obtained from the UCNPs cores of this multifunctional drug delivery system. The result showed that our system of DOX@UCNP@mSiO$_2$–AuNRs has the excellent synergistic therapy ability. And the therapeutic effect of this system is better than the system which has the monotherapy function only. With these properties of synergistic therapy and tumor imaging, we envisioned that our work will provide a significant methodology for development of multifunctional nanocarrier for diverse applications in the area of synergistic therapy and imaging.

Notes and references

1 T. Zheng, G. Li, F. Zhou, R. Wu, J. Zhu and H. Wang, *Adv. Mater.*, 2016, **28**, 8218–8226.
2 W. Sun, T. Jiang, Y. Lu, M. Reiff, R. Mo and Z. Gu, *J. Am. Chem. Soc.*, 2014, **136**, 14722–14725.
3 D. Zhao, J. Xu, X. Yi, Q. Zhang, S. Cheng, R. Zhuo and F. Li, *ACS Appl. Mater. Interfaces*, 2016, **8**, 14845–14854.
4 T. Sun, Y. S. Zhang, B. Pang, D. C. Hyun, M. Yang and Y. Xia, *Angew. Chem., Int. Ed.*, 2014, **53**, 12320–12364.
5 A. Y. Ammar, D. Sierra, F. Mérola, N. Hildebrandt and X. L. Guével, *ACS Nano*, 2016, **10**, 2591–2599.
6 J. Wu, X. He, P. Jiang, M. Gong, R. Zhuo and S. Cheng, *RSC Adv.*, 2016, **6**, 69083–69093.
7 T. Sun, Y. Zhu, F. Chen, C. Qi, B. Lu, J. Wu, D. Zhou and C. Zhang, *RSC Adv.*, 2016, **6**, 103399–103411.
8 Y. Wang, M. S. Shim, N. S. Levinson, H.-W. Sung and Y. Xia, *Adv. Funct. Mater.*, 2014, **24**, 4206–4220.
9 R. G. Chaudhuri and S. Paria, *Chem. Rev.*, 2012, **112**, 2373–2433.
10 H. Meng, M. Wang, H. Liu, X. Liu, A. Situ, B. Wu, Z. Ji, C. H. Chang and A. E. Nel, *ACS Nano*, 2015, **9**, 3540–3557.
11 D. Babikova, R. Kalinova, L. Zhelezova, D. Momekova, S. Konstantinov, G. Momekov and L. Dimitrov, *RSC Adv.*, 2016, **6**, 84634–84644.
12 P. Huang, B. Zeng, Z. Mai, J. Deng, Y. Fang, W. Huang, H. Zhang, J. Yuan, Y. Wei and W. Zhou, *J. Mater. Chem. B*, 2016, **4**, 46–56.
13 Y. Zhao, Z. Luo, M. Li, Q. Qu, X. Ma, S. Yu and Y. Zhao, *Angew. Chem., Int. Ed.*, 2015, **54**, 919–922.
14 C. Li, T. Chen, L. Ocsoy, G. Zhu, E. Yasun, M. You, C. Wu, J. Zheng, E. Song, C. Huang and W. Tan, *Adv. Funct. Mater.*, 2014, **24**, 1772–1780.
15 M. Yin, E. Ju, Z. Chen, Z. Li, J. Ren and X. Qu, *Chem.–Eur. J.*, 2014, **20**, 14012–14017.
16 L. Xiong, J. Bi, Y. Tang and S. Qiao, *Small*, 2016, **12**, 4735–4742.
17 X. Wu, F. Tian, W. Wang, J. Chen, M. Wu and J. X. Zhao, *J. Mater. Chem. C*, 2013, **1**, 4676–4684.
18 G. Luo, W. Chen, Q. Lei, W. Qiu, Y. Liu, Y. Cheng and X. Zhang, *Adv. Funct. Mater.*, 2016, **2016**(26), 4339–4350.
19 J. Liu, W. Bu and J. Shi, *Acc. Chem. Res.*, 2015, **48**, 1797–1805.
20 W. Q. Li, S. Z. F. Phua, H. V. Xu, S. Sreejithb and Y. Zhao, *Nanoscale*, 2016, **8**, 12510–12519.
21 M. Wu, Q. Meng, Y. Chen, L. Zhang, M. Li, X. Cai, Y. Li, P. Yu, L. Zhang and J. Shi, *Adv. Mater.*, 2016, **28**, 1963–1969.
22 G. Song, Q. Wang, Y. Wang, G. Lv, C. Li, R. Zou, Z. Chen, Z. Qin, K. Huo, R. Hu and J. Hu, *Adv. Funct. Mater.*, 2013, **23**, 4281–4292.
23 J. Yang, L. Fan, F. Wang, Y. Luo, X. Sui, W. Li, X. Zhang and Y. Wang, *Nanoscale*, 2016, **8**, 9537–9547.
24 Y. Wang and H. Gu, *Adv. Mater.*, 2015, **27**, 576–585.

25 S. Giret, M. W. C. Man and C. Carcel, *Chem.–Eur. J.*, 2015, **21**, 13850–13865.

26 S. Wu and H.-J. Butt, *Adv. Mater.*, 2016, **28**, 1208–1226.

27 C. Wang, L. Cheng, Y. Liu, X. Wang, X. Ma, Z. Deng, Y. Li and Z. Liu, *Adv. Funct. Mater.*, 2013, **23**, 3077–3086.

28 Q. Xiao, X. Zheng, W. Ge, S. Zhang, F. Chen, H. Xing, Q. Ren, W. Fan, K. Zhao, Y. Hua and J. Shi, *J. Am. Chem. Soc.*, 2013, **135**, 13041–13048.

29 J. Liu, W. Bu and J. Shi, *Acc. Chem. Res.*, 2015, **48**, 1797–1805.

30 N. M. Idris, M. K. G. Jayakumar, A. Bansalab and Y. Zhang, *Chem. Soc. Rev.*, 2015, **44**, 1449–1478.

31 D. Wang, L. Zhu, J. Chen and L. Dai, *Angew. Chem., Int. Ed.*, 2016, **55**, 1–6.

32 J. Liu, W. Bu, L. Pan and J. Shi, *Angew. Chem., Int. Ed.*, 2013, **52**, 4375–4379.

33 S. He, K. Krippes, S. Ritz, Z. Chen, A. Best, H.-J. Butt, V. Mailänderab and S. Wu, *Chem. Commun.*, 2015, **51**, 431–434.

34 V. Shanmugam, S. Selvakumar and C.-S. Yeh, *Chem. Soc. Rev.*, 2014, **43**, 6254–6287.

35 L. Zhang, Y. Chen, Z. Li, L. Li, P. S. Cricq, C. Li, J. Lin, C. Wang, Z. Su and J. I. Zink, *Angew. Chem., Int. Ed.*, 2016, **55**, 2118–2121.

36 R. M. Fratila, S. R. Fernández and J. M. Fuente, *Nanoscale*, 2015, **7**, 8233–8260.

37 M. Zhou, R. Zhang, M. Huang, W. Lu, S. Song, M. P. Melancon, M. Tian, D. Liang and C. Li, *J. Am. Chem. Soc.*, 2010, **132**, 15351–15358.

38 S. Tang, M. Chen and N. Zheng, *Small*, 2014, **10**, 3139–3144.

39 M. Sun, L. Xu, W. Ma, X. Wu, H. Kuang and L. Wang, *Adv. Mater.*, 2016, **28**, 898–904.

40 Y. Liu, M. Yang, J. Zhang, X. Zhi, C. Li, C. Zhang, F. Pan, K. Wang, Y. Yang, J. M. Fuentea and D. Cui, *ACS Nano*, 2016, **10**, 2375–2385.

41 Z. Zhang, J. Wang, X. Nie, T. Wen, Y. Ji, X. Wu, Y. Zhao and C. Chen, *J. Am. Chem. Soc.*, 2014, **136**, 7317–7326.

42 Z. Li, H. Huang, S. Tang, Y. Li, X. Yu, H. Wang, P. Li, Z. Sun, H. Zhang, C. Liu and P. K. Chu, *Biomaterials*, 2016, **74**, 144–154.

43 J. Song, P. Huang, H. Duan and X. Chen, *Acc. Chem. Res.*, 2015, **48**, 2506–2515.

44 A. Gharatape, M. Milani, S. H. Rasta, M. P. Moghaddam, S. A. Kandjani, S. Davaran and R. Salehi, *RSC Adv.*, 2016, **6**, 110499–110510.

45 Z. Zhang, C. Liu, J. Bai, C. Wu, Y. Xiao, Y. Li, J. Zheng, R. Yang and W. Tan, *ACS Appl. Mater. Interfaces*, 2015, **7**, 6211–6219.

46 S. Shen, H. Tang, X. Zhang, J. Ren, Z. Pang, D. Wang, H. Gao, Y. Qian, X. Jiang and W. Yang, *Biomaterials*, 2013, **34**, 3150–3158.

47 M. Chen, P. Qiu, X. He, K. Wang, S. Chen, S. Yang and X. Ye, *J. Mater. Chem. B*, 2014, **2**, 3204–3213.

48 E. Ju, Z. Li, Z. Liu, J. Ren and X. Qu, *ACS Appl. Mater. Interfaces*, 2014, **6**, 4364–4370.

49 W. Fan, B. Shen, W. Bu, F. Chen, K. Zhao, S. Zhang, L. Zhou, W. Peng, Q. Xiao, H. Xing, J. Liu, D. Ni, Q. He and J. Shi, *J. Am. Chem. Soc.*, 2013, **135**, 6494–6503.

50 S. Baek, R. K. Singh, T.-H. Kim, J.-W. Seo, U. S. Shin, W. Chrzanowski and H.-W. Kim, *ACS Appl. Mater. Interfaces*, 2016, **8**, 8967–8979.

51 Y. Chang, P. Liao, H.-S. Sheu, Y.-J. Tseng, F.-Y. Cheng and C.-S. Yeh, *Adv. Mater.*, 2012, **24**, 3309–3314.

52 N. Li, Z. Yu, W. Pan, Y. Han, T. Zhang and B. Tang, *Adv. Funct. Mater.*, 2013, **23**, 2255–2262.